PAPER

Enhancing perovskite solar cell performance and stability by doping barium in methylammonium lead halide†

Shun-Hsiang Chan,[a] Ming-Chung Wu, [iD] *[abc] Kun-Mu Lee,[abc] Wei-Cheng Chen,[a] Tzu-Hao Lin[a] and Wei-Fang Su*[d]

Organic–inorganic lead halide perovskite solar cells are considered as one of the most promising technologies for future photovoltaics because they show high power conversion efficiency (PCE) and can be fabricated through a simple solution process. Non-toxic alkaline-earth metal cations are suitable candidates to replace toxic lead in perovskite because they maintain the charge balance in perovskite and some of them meet the tolerance factor of Goldschmidt's rule. We investigated four kinds of alkaline-earth metal cations (Mg^{2+}, Ca^{2+}, Sr^{2+}, and Ba^{2+}) to replace lead cations partially. Among these four alkaline-earth metals, the Ba^{2+} is most suitable for Pb^{2+} replacement in perovskite films and exhibits the best power conversion efficiency. Furthermore, we systematically studied the crystal structure, absorption behavior and surface morphology of Ba^{2+}-doped perovskite films with different doping levels. The relationship between the charge carrier dynamics and Ba^{2+} concentration was evaluated by the time-resolved photoluminescence (TRPL) technique. The Ba^{2+}-doped perovskite films that can be processed in the environment containing moisture (1.0% relative humidity) are stable. At the optimal 3.0 mol% Ba^{2+} replacement, the PCE of the fabricated solar cell is increased from 11.8 to 14.0%, and the PCE of champion devices is as high as 14.9% with increased storage stability.

1. Introduction

The organic–inorganic lead halide perovskite solar cell (PSC) is considered as one of the most promising photovoltaic technologies due to its rapid progress in power conversion efficiency (PCE).[1–4] In 2009, T. Miyasaka *et al.* were the first group to have reported the fabrication of PSCs from high visible absorbance $CH_3NH_3PbI_3$ and a PCE of 3.8% was obtained.[5] After that, many research groups have been devoted to the development of PSCs, and the high PCE of 22.1% is achieved.[6] The typical structure of the organic–inorganic lead halide perovskite is $APbX_3$, where A is an organic cation and X is a halide.[7] However, long-term contact with lead can cause severe nerve and brain damage.[8] The toxicity issue of lead drags the commercialization of PSCs.

To advance the technology of PSCs, the development of lead-reduced or lead-free perovskite is imperative.[9–14]

N. K. Noel *et al.* and F. Hao *et al.* demonstrated a tin-based perovskite ($CH_3NH_3SnX_3$) solar cell.[9,11,15] However, the device exhibited a PCE of 6.4%, low stability, and low reproducibility as Sn^{2+} readily oxidizes to Sn^{4+}.[15,16] Partial replacement (doping) to reduce the lead in lead halide perovskite has been studied. For instance, an aluminum (Al)-doped perovskite film improves the device performance because the crystal quality is increased and the microstrain is reduced in the perovskite film.[17] J. Navas *et al.* partially replaced Pb with Sn, Sr, Cd, and Ca.[18] They found that Sr^{2+}-doped and Ca^{2+}-doped perovskites have a smaller bandgap compared with that of $CH_3NH_3PbI_3$ (1.57 eV). The perovskite with a lower bandgap could extend the range of light absorption and increase the amount of photocurrent.[16] D. Pérez-del-Rey *et al.* described that the partial replacement of Pb^{2+} with Sr^{2+} can improve the surface morphology of the perovskite film which can thus enhance the charge transport efficiency for high current density and high fill factors.[19]

M. Pazoki *et al.* reported the structure simulation of alkaline-earth metal perovskites ($CH_3NH_3CaI_3$, $CH_3NH_3SrI_3$, and $CH_3NH_3BaI_3$) based on Goldschmidt's rule and the quantum mechanism.[20] The simulated bandgaps of alkaline-earth metal perovskites are too high to be an efficient photo-absorber.[21] However, alkaline-earth metal perovskites have a stable perovskite structure.[20,22,23] Thus, we partially replace the lead with

[a] Department of Chemical and Materials Engineering, Chang Gung University, Taoyuan 33302, Taiwan. E-mail: mingchungwu@mail.cgu.edu.tw; Fax: +886 3 3775580; Tel: +886 3 2118800 extn 3545

[b] Center for Reliability Sciences & Technologies, Chang Gung University, Taoyuan 33302, Taiwan

[c] Division of Neonatology, Department of Pediatrics, Chang Gung Memorial Hospital, Taoyuan 33305, Taiwan

[d] Department of Materials Science and Engineering, National Taiwan University, Taipei 10617, Taiwan. E-mail: suwf@ntu.edu.tw; Fax: +886 2 23634562; Tel: +886 2 33664078

† Electronic supplementary information (ESI) available. See DOI: 10.1039/c7ta05720b

alkaline-earth metals to have a structure of $CH_3NH_3M_{1-x}Pb_x$-$I_{3-y}Cl_y$, where M represents alkaline-earth metals (Mg, Ca, Sr and Ba). After a systematic study, it was found that the Ba^{2+}-doped perovskite (i.e., $CH_3NH_3Ba_{1-x}Pb_xI_{3-y}Cl_y$) exhibits the highest photovoltaic performance. We investigated the crystal structure, absorption behavior and surface morphology of various Ba^{2+}-doped perovskite active layers with different doping levels, and determined the correlation between these properties and Ba^{2+} doping levels. The charge carrier dynamics of various Ba^{2+}-doped perovskite active layers were also explored by time-resolved photoluminescence (TRPL) spectroscopy. The photovoltaic performances of various Ba^{2+}-doped PSCs with different doping levels are elucidated systemically.

2. Experimental details

• Materials and sample preparation

Methylammonium iodide (CH_3NH_3I, MAI) was synthesized based on our previous study.[24] Briefly, 30.0 mL of hydriodic acid (HI, >57.0 wt% aqueous solution, Sigma-Aldrich) was added dropwise into the methylamine solution (CH_3NH_2, 33.0 wt% in ethanol, Sigma-Aldrich) with continuous stirring at 0 °C for 2 h. A blue-green solution was obtained, which was then rotary evaporated at 60 °C for 30 min to get a white precipitate. Subsequently, the white precipitate was dissolved in ethanol and was recrystallized in diethyl ether. Finally, the MAI powder was dried at 50 °C in a vacuum oven for 24 h. The various alkaline-earth metal-doped perovskite precursor solution was prepared by mixing MAI powder, lead chloride ($PbCl_2$, 99.999%, Sigma-Aldrich), and different metal iodides, including magnesium iodide (MgI_2, 98%, Sigma-Aldrich), calcium iodide (CaI_2, 99%, Sigma-Aldrich), strontium iodide (SrI_2, >99.99, Sigma-Aldrich), and barium iodide (BaI_2, 99.995%, Sigma-Aldrich), with various stoichiometric ratios at 0.9 M in 1.0 mL of dimethylformamide ($HCON(CH_3)_2$, DMF, anhydrous, 99.8%, ACROS). For the preparation of TiO_2 precursor solution, 375.0 μL of titanium isopropoxide ($Ti(OCH(CH_3)_2)_4$, TTIP, >97%, Sigma-Aldrich) was added dropwise into 2.5 mL of ethanol (C_2H_5OH, 99.5%, Shimakyu's Pure Chemicals). A 35.0 μL of 2.0 M HCl aqueous solution was added dropwise into 2.5 mL of ethanol in another beaker, and then it was added to the Ti precursor solution in an ice-bath with continuous stirring for 30 min. For the preparation of precursor solution for the hole transport layer, a 2,2′,7,7′-tetrakis[N,N-di(4-methoxyphenyl)amino]-9,9′-spirobifluorene (spiro-OMeTAD, FrontMaterials Co. Ltd.) solution was synthesized according to a previous report.[25] The lithium-bis-(trifluoromethanesulfonyl)imide (Li-TFSI, 99.95%, Sigma-Aldrich) of 104 mg was dissolved in 200.0 μL of acetonitrile (CH_3CN, 99.5%, ACROS). The spiro-OMeTAD solution was well prepared by dissolving 80 mg of spiro-OMeTAD, 28.5 μL of 4-tert-butylpyridine (tBP, 96%, Sigma-Aldrich), and 17.5 μL of Li-TFSI solution in 1.0 mL of chlorobenzene (C_6H_5Cl, CB, 99.8%, ACROS) with continuous stirring for 30 min. The series of perovskite solution and spiro-OMeTAD solution were prepared in a chamber of N_2 with 1.0% RH. All chemicals were used as received without any purification.

• Fabrication of solar cells

The FTO glass (7 Ω, FrontMaterials Co. Ltd.) was cleaned sequentially with detergent, ammonia/hydrogen peroxide solution, methanol, and isopropanol by using an ultrasonic cleaner. The FTO glass was treated in a UV-ozone for 20 min. The TiO_2 precursor solution was spin-coated on the FTO glass by 1000 rpm for 40 s and calcined at 550 °C for 30 min to form a TiO_2 electron transport layer. Then, various alkaline-earth metal-doped perovskite precursor solutions were spin-coated on the TiO_2 coated FTO glass by 1200 rpm for 45 s in a N_2 chamber with 1.0% RH, and the coated samples were annealed at 100 °C for 60 min. Subsequently, the spiro-OMeTAD solution was spin-coated over a perovskite layer at 4000 rpm for 30 s. Finally, 100 nm of gold electrode was thermally evaporated on the device surface through a shadow mask with an 0.09 cm^2 active area. The performance of devices fabricated from different perovskite layers was evaluated by measuring 15 separated solar cells and expressed in statistical average.

• Characterization of materials and devices

The surface and cross-sectional morphology of the perovskite film was studied by SEM (SNE-4500M, SEC). The surface roughness of the perovskite film was analyzed by AFM (Bruner Multimode2-U-NSV, Bruker) in the tapping mode. The chemical compositions of the perovskite films were investigated by energy dispersive spectroscopy (EDS) (INCA Penta FET-x3, Oxford Instruments). The UV-visible absorption spectra were obtained with a UV-vis spectrometer (V-730, Jasco). The crystal structure was determined with a X-ray diffractometer (D2 phaser, Bruker). For the photoluminescence (PL) measurement, the samples were excited with a 440 nm continuous-wave diode laser (PDLH-440-25, DongWoo Optron Co. Ltd.) with a 550 nm longpass filter. The emission spectrum was collected and analyzed using a photomultiplier tube detector system (PDS-1, DongWoo Optron Co. Ltd.) and conventional photon-counting electronics using a monochromator (Monora 150i, DongWoo Optron Co. Ltd.). For TRPL spectroscopy, a 440 nm pulse laser operating at 312.5 MHz, with a 1.08 μs duration was used for excitation. The TRPL spectra were measured using a time-correlated single photon counting spectrometer (WELLS-001 FX, DongWoo Optron Co. Ltd.). The current density–voltage (J–V) characteristic of the device was measured under solar-simulated AM1.5 sunlight irradiation (Newport-69920, 100 mW cm^{-2}) calibrated with a silicon reference cell (Oriel P/N 91150 V, VLSI standards) with a KG-5 visible color filter. The external quantum efficiency (EQE) was measured with an IPCE spectrometer (EQE-R-3011, Enli Technology Co. Ltd). It was calibrated with a single-crystal silicon reference cell for each EQE measurement.

3. Results and discussion

The four kinds of alkaline-earth metal cations at 3.0 mol%, including Mg^{2+}, Ca^{2+}, Sr^{2+}, and Ba^{2+}, were doped into the perovskite film, and their corresponding XRD patterns are shown in Fig. 1. The incomplete phase transformation and PbI_2 existence are observed for the pristine, Mg^{2+}, Ca^{2+}, and
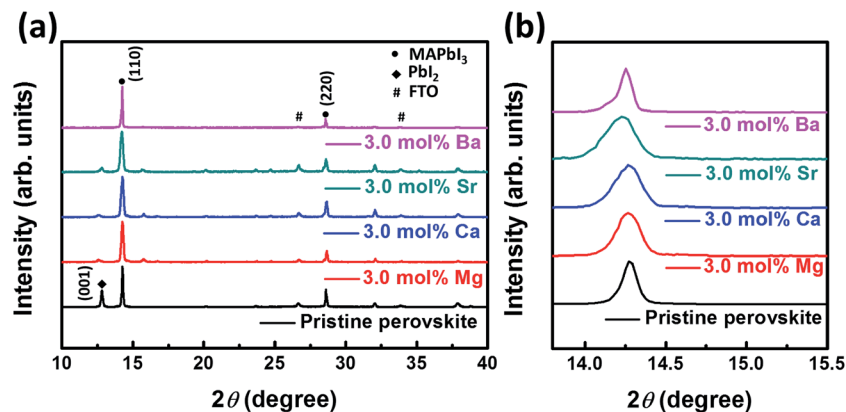
Fig. 1 (a) XRD patterns of the perovskite film without and with alkaline-earth metal doping, and (b) the magnified XRD patterns in the range of 2θ between 13.8–15.5 degrees at the plane of (110).

Sr^{2+}-doped films as shown in Fig. 1(a).[26,27] In contrast, the film doped with Ba^{2+} shows the inconspicuous PbI_2 (001) peak because it almost transforms into perovskite. Fig. 1(b) exhibits the magnified XRD patterns of the perovskite film (110) plane. The 3.0 mol% Ba^{2+}-doped perovskite film shows a slight shift to the smaller scattering angles due to the ionic radius of Ba^{2+} (~135 pm) which is larger than that of Pb^{2+} (~119 pm). The average crystallite size was estimated from the full-width at half maximum of the perovskite film (110) peak by using the Scherrer equation. The 3.0 mol% Ba^{2+}-doped perovskite film shows the largest crystallite size of ~91.0 nm among all alkaline-earth metal doped films. These results indicated that Ba^{2+} is compatible with the perovskite structure. For the pristine perovskite film, the crystallite size is merely ~75.5 nm. The large crystallite size could enhance the transport of charge carriers, and thus increases the photocurrent and PCE of perovskite devices.[28,29]

Fig. 2 shows the surface microstructures of the perovskite film without and with dopants. The pristine perovskite film presents some small pinholes on the film surface (Fig. 2(a)). The Mg^{2+}-doped perovskite film is rough when the Mg^{2+} concentration reaches 3.0 mol% (Fig. 2(b)). The ionic radius of Mg^{2+} is too small to fit the tolerance factor of Goldschmidt's rule, and the octahedral structure of $CH_3NH_3MgI_3$ is outside of the range as shown in Fig. S1.†[30–32] The films doped with Ca^{2+} and Sr^{2+} exhibit some pinholes as shown in Fig. 2(c) and (d).[18] In contrast, the Ba^{2+}-doped film appears to have the most homogeneous distribution (Fig. 2(e)). Thus, we expect that the solar cell fabricated from the Ba^{2+}-doped film could present high photovoltaic performance, whereas, the PSCs fabricated from the Mg^{2+}-doped film could show the worst device performance.

Fig. 3(a) shows the red-shift of the absorption spectra after the film was doped with Ba^{2+}. Fig. 3(b) shows the Tauc plots of the film with and without Ba^{2+} doping. The bandgaps of the
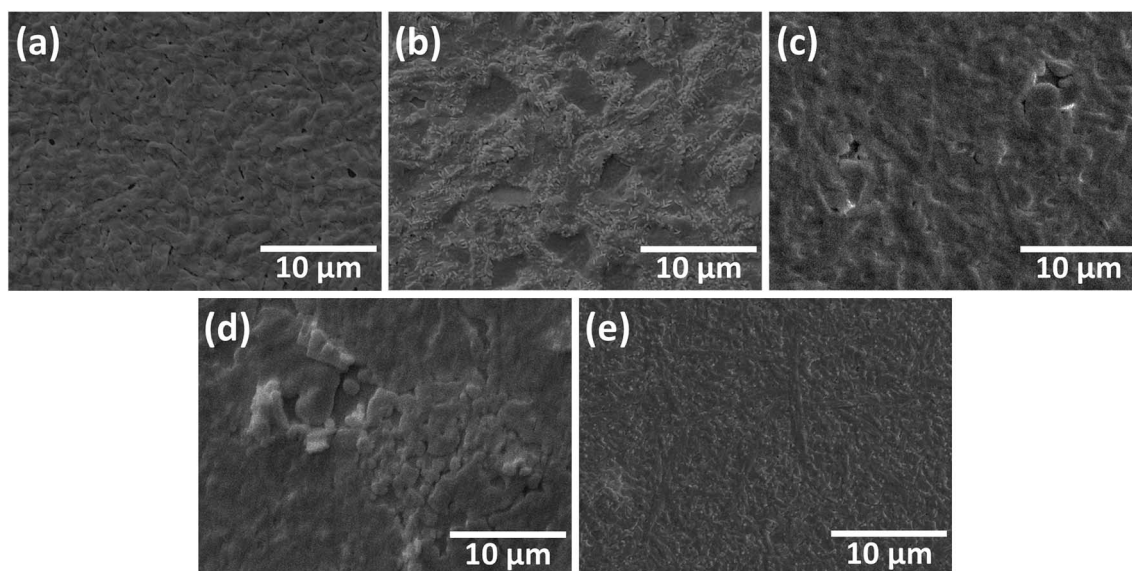

Fig. 2 SEM images of (a) the pristine perovskite film, (b) 3.0 mol% Mg^{2+}-doped perovskite film, (c) 3.0 mol% Ca^{2+}-doped perovskite film, (d) 3.0 mol% Sr^{2+}-doped perovskite film, and (e) 3.0 mol% Ba^{2+}-doped perovskite film.
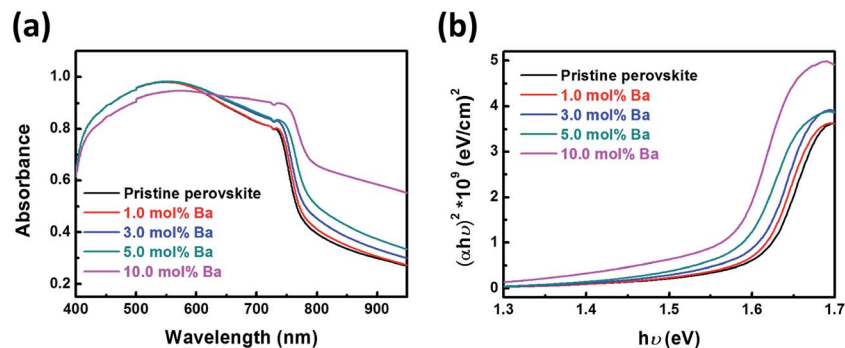
Fig. 3 (a) Absorption spectra and (b) Tauc plots of the pristine perovskite film and various Ba^{2+}-doped perovskite films with different doping levels.

films can be estimated from the absorption spectrum. They are decreased by increasing the amount of the dopant to be 1.62, 1.60, 1.59, 1.58 and 1.57 eV for 0.0, 1.0, 3.0, 5.0 and 10.0 mol%, respectively. The results are related to the crystalline structure, microstructure, and doping level. The report of J. Navas *et al.* indicated that the bandgap energy of perovskite materials decreased slightly, suggesting that the presence of the dopants slightly modified the interaction with the ions in the network, leading to changes in the bandgap.[18] As the bandgap of the Ba^{2+}-doped perovskite film is decreased with an increasing doping level, it can extend the adsorption range and improve the photocurrent.[16]

The correlation between the crystal structure and the Ba^{2+} doping level is studied systemically. Fig. 4(a) shows the XRD patterns of perovskite films with different doping concentrations of Ba^{2+}. When the doping level is >1.0 mol%, the PbI_2 (001) peak disappears, and the typical tetragonal $CH_3NH_3PbI_3$ perovskite film is formed. Fig. 4(b) indicates that the (110) peaks of the tetragonal $CH_3NH_3PbI_3$ perovskite film are shifted to smaller scattering angles due to the ionic radius of Ba^{2+} (~135 pm) which is larger than that of Pb^{2+} (~119 pm). Fig. 4(c) is the plot of the calculated crystallite size of various Ba^{2+}-doped perovskite films. When the Ba^{2+} doping level is increased from

0.0 to 3.0 mol%, the crystallite size gradually increases from 75.5 to 91.0 nm. However, the crystallite size is reduced to 79.2 nm as the doping level is increased to 10.0 mol%. These results are due to non-uniform strain (microstrain).[17] It is known that the crystallite size is related to the rate of carrier transport. A larger crystallite size presents a higher carrier transport rate. Thus, the performance of the device is improved due to the increased current density.[33] In addition, when the Ba^{2+} doping level is increased to >10.0 mol% (Fig. S2†), the BaI_2 peak appears because of the excess amount of the Ba dopant.[34] Hence, we adopted 10.0 mol% as the critical Ba^{2+} concentration.

Fig. 5(a–e) illustrate the SEM images of various perovskite films without and with various doping levels. The pristine perovskite film contains many pinholes and voids (~300 nm) on the surface (Fig. 5(a)). However, the voids are gradually reduced when the Ba^{2+} doping level is increased to 1.0 mol% (Fig. 5(b)). At 3.0 mol% and 5.0 mol% Ba^{2+} doping levels, their surface morphologies appear more homogeneous (Fig. 5(c and d)) than that of the 1.0 mol% sample. However, when the Ba^{2+} doping level reaches 10.0 mol%, the film becomes rough again (Fig. 5(e)). To further discuss the surface morphology of various Ba^{2+}-doped perovskite films, we used AFM to measure the surface roughness of each film and the results are shown in
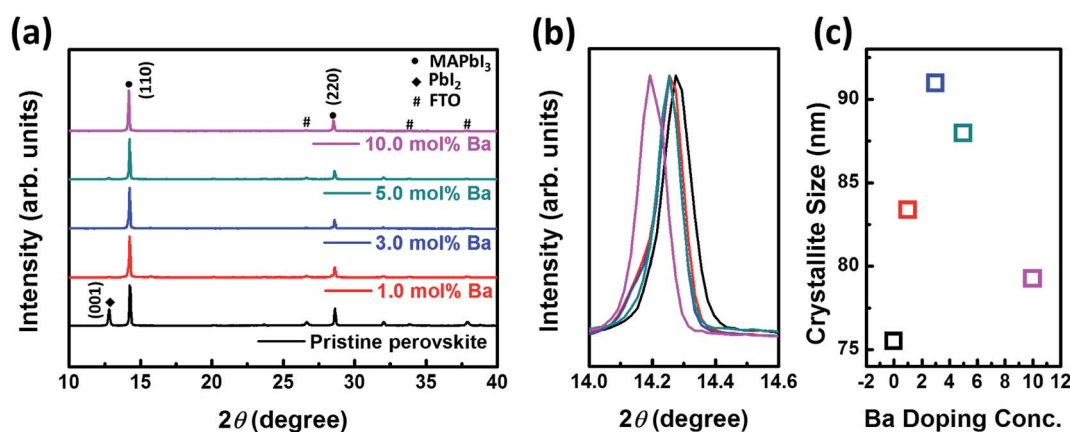

Fig. 4 (a) XRD patterns of perovskite films without and with Ba^{2+} doping, (b) the magnified XRD patterns at 2θ between 14.0–14.6 degrees, and (c) the calculated crystallite sizes of perovskite films without and with Ba^{2+} doping.

This journal is © The Royal Society of Chemistry 2017

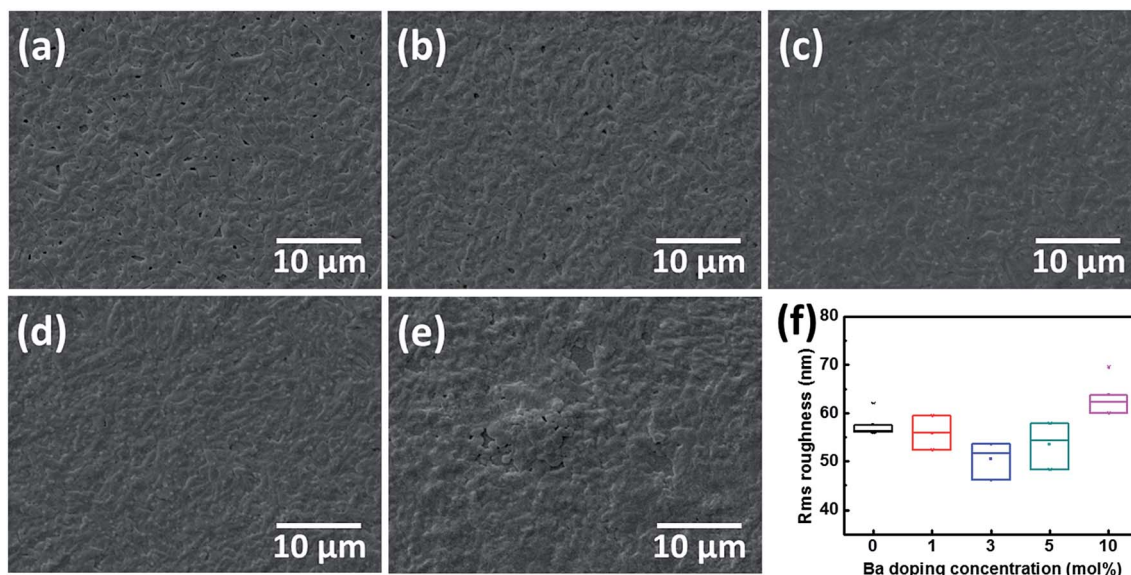J. Mater. Chem. A, 2017, 5, 18044–18052 | 18047

Fig. 5 SEM images of (a) the pristine perovskite film, (b) 1.0 mol%, (c) 3.0 mol%, (d) 5.0 mol%, and (e) 10.0 mol% Ba^{2+}-doped perovskite films. (f) The R_q distribution of various perovskite films was measured by AFM.

Fig. S3 of the ESI.† The root mean square roughness (R_q) is slightly decreased from 57.6 to 50.4 nm with increasing the Ba^{2+} doping level from 0.0 to 3.0 mol% (Fig. 5(f)). However, the R_q of the 10.0 mol% Ba-doped perovskite film is increased to 63.9 nm due to the formation of voids from an excess amount of Ba^{2+}.

The charge carrier dynamics of the Ba-doped perovskite device are investigated by using PL and TRPL spectroscopy. The various Ba-doped perovskite/TiO$_2$/FTO films were measured by the static PL (Fig. 6(a)) and transient PL decay (Fig. 6(b)). Fig. 6(a) shows the PL intensity which is decreased with a low doping level of 3.0 mol% but is increased with a high doping level of 10.0 mol%. The decrease of the PL intensity is attributed to the efficient electron extraction that occurred in the perovskite/TiO$_2$ interface due to high coverage of the perovskite film. The increase of the PL intensity is attributed to an inhomogeneous and partially covered perovskite film.[35] To check the charge transfer rate and the charge separation efficiency, the transient PL decay plots of different films were established by

time-correlated single photon counting (TCSPC). The transient PL decay curve can be fitted by a bi-exponential decay function as below,

$$F(t) = A_1 \exp\left(-\frac{t}{\tau_1}\right) + A_2 \exp\left(-\frac{t}{\tau_2}\right)$$

where A_1 and A_2 are the time independent coefficients of amplitude fraction, respectively. τ_1 and τ_2 are the fast decay time and slow decay time, respectively. The average decay time was calculated using the following equation:

$$\tau_{avg} = \sum_i A_i \tau_i \bigg/ \sum_i A_i$$

The measured fast decay time (τ_1), slow decay time (τ_2), and PL average lifetime (τ_{avg}) of Ba^{2+}-doped perovskite films are summarized in Table 1. The fast decay component is the result of free carriers quenching in the perovskite film close to the
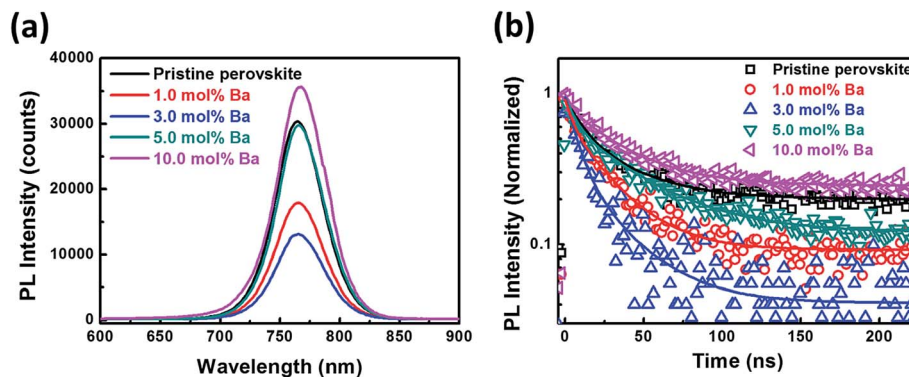

Fig. 6 (a) Photoluminescence spectra and (b) time-resolved photoluminescence characterization of perovskite films without and with various amounts of Ba^{2+} doping.

Table 1 Summary of the measured fast decay time (τ_1), slow decay time (τ_2), and PL average decay (τ_{avg}) of the films of Ba^{2+}-doped perovskite/TiO$_2$/FTO

Sample name	A_1 (%)	τ_1 (ns)	A_2 (%)	τ_2 (ns)	τ_{avg} (ns)
Pristine perovskite	58.2	14.2	41.8	40.3	25.0
1.0 mol% Ba^{2+}-doped perovskite	60.2	13.9	39.8	36.4	22.9
3.0 mol% Ba^{2+}-doped perovskite	66.0	7.7	34.0	29.4	15.0
5.0 mol% Ba^{2+}-doped perovskite	41.6	4.4	58.4	36.2	22.9
10.0 mol% Ba^{2+}-doped perovskite	29.3	8.3	70.7	39.9	30.6

TiO$_2$ compact layer, and the slow decay component is the result of charge recombination.[36,37] For the pristine perovskite film, the fast decay time is 14.2 ns, the slow decay lifetime is 40.3 ns and their corresponding amplitudes are 58.2% and 41.8%, respectively. On the other hand, the fast decay lifetime of the 3.0 mol% Ba^{2+}-doped perovskite film significantly decreased to 7.7 ns and the amplitude increases from 58.2 to 66.0%. That results in improved charge transport efficiency to the TiO$_2$ compact layer and reduced electron–hole recombination. The average lifetime of pristine perovskite is 25.0 ns and is reduced to 15.0 ns for the 3.0 mol% Ba^{2+}-doped perovskite film. The shortest PL average decay time of the 3.0 mol% Ba^{2+}-doped perovskite film is due to the improved surface morphology and enlarged crystallite size of the perovskite film. The fast charge transport and the reduced charge recombination are necessary for the high-performance PSC.[38] We also compare the PL spectra and TRPL decay of the perovskite film with/without the TiO$_2$ quencher. Two kinds of schematic diagram of the device are shown in Fig. S4(a and d).† The PL intensity of the sample without the quencher (Fig. S4(b)†) exhibits the opposite trend to that with the quencher (Fig. S4(e)†). The PL intensity of the 3.0 mol% Ba-doped perovskite film is higher than that of the pristine perovskite film (Fig. S4(b)†). The high PL intensity indicates that the more electron–hole pairs in the perovskite film result in the stronger radiative recombination.[17,39] The average PL lifetimes of the pristine perovskite and 3.0 mol% Ba-doped

perovskite are 30.2 ns and 44.6 ns, respectively (Fig. S4(c)†). The average PL lifetime of the sample without the quencher is higher than that of the sample with the quencher (Fig. S4(f)†).

The photovoltaic characteristics of solar cells fabricated from perovskite films with and without alkaline-earth metal dopants are listed in Table 2 in detail. The average PCE of a PSC with the pristine perovskite active layer is about 11.8%. The PCE of the PSC with the Mg^{2+} and Sr^{2+}-doped perovskite active layer decreases with increasing the doping levels. The 1.0 mol% Ca^{2+}-doped PSC shows a PCE of 12.0% that is close to that of the pristine PSC. As stated above, the PCE of the Ba^{2+}-doped PSC is higher than that of other alkaline-earth metal-doped PSCs.

Fig. 7(a) shows the cross-sectional SEM image of the Ba^{2+}-doped PSC, and it has the configuration of FTO/TiO$_2$/Ba^{2+}-doped perovskite/spiro-OMeTAD/Au electrode. The thicknesses of the TiO$_2$ compact layer, perovskite film, and spiro-OMeTAD are 60, 600, and 520 nm, respectively. In this study, the 3.0 mol% Ba^{2+}-doped PSC exhibits the highest PCE of 14.0% (Table 2). Thus, we further discussed the optical property and crystal structure of the 3.0 mol% Ba^{2+}-doped perovskite film. The absorption spectra of the 3.0 mol% Ba-doped perovskite film with different annealing temperatures are shown in Fig. S5(a).† The absorbance of the 3.0 mol% Ba^{2+}-doped perovskite film increases with increasing the annealing temperature from 80 to 100 °C. The result indicates that annealing the perovskite film at 80 °C cannot form the perovskite completely.[40] The perovskite

Table 2 Characteristics of the pristine perovskite film and various alkaline-earth metal-doped PSCs

| Sample name	Doping conc.	J_{sc} (mA cm^{-2})	V_{oc} (V)	FF (%)	PCE (%)
Pristine perovskite	0.0	19.2 ± 0.5	0.95 ± 0.03	65.0 ± 1.1	11.8 ± 0.6
Mg^{2+}-doped perovskite	1.0	18.7 ± 0.6	0.89 ± 0.01	64.8 ± 0.8	10.8 ± 0.4
	3.0	15.1 ± 1.0	0.87 ± 0.10	57.0 ± 2.7	7.5 ± 1.1
	5.0	10.4 ± 0.8	0.80 ± 0.02	60.7 ± 5.2	5.1 ± 0.5
	10.0	6.5 ± 0.4	0.58 ± 0.07	42.3 ± 5.8	1.6 ± 0.4
Ca^{2+}-doped perovskite	1.0	18.4 ± 0.6	0.96 ± 0.01	67.8 ± 1.8	12.0 ± 0.4
	3.0	17.1 ± 0.7	0.95 ± 0.02	65.9 ± 3.2	10.6 ± 0.5
	5.0	17.0 ± 1.0	0.80 ± 0.05	60.8 ± 3.5	8.3 ± 0.7
	10.0	1.4 ± 0.3	0.72 ± 0.02	42.3 ± 2.6	0.4 ± 0.1
Sr^{2+}-doped perovskite	1.0	18.6 ± 0.5	0.93 ± 0.02	65.0 ± 2.5	11.2 ± 0.3
	3.0	18.4 ± 0.3	0.90 ± 0.01	64.7 ± 2.7	10.7 ± 0.1
	5.0	18.4 ± 0.6	0.81 ± 0.02	64.3 ± 2.2	9.6 ± 0.3
	10.0	3.9 ± 0.3	0.61 ± 0.03	41.8 ± 3.5	1.0 ± 0.1
Ba^{2+}-doped perovskite	1.0	19.5 ± 0.8	0.98 ± 0.01	68.8 ± 1.2	13.1 ± 0.5
	3.0	20.4 ± 0.3	0.99 ± 0.01	69.6 ± 1.6	14.0 ± 0.5
	5.0	19.3 ± 0.7	0.96 ± 0.02	67.2 ± 2.9	12.4 ± 0.5
	10.0	17.0 ± 0.9	0.85 ± 0.02	61.1 ± 2.8	8.8 ± 0.3
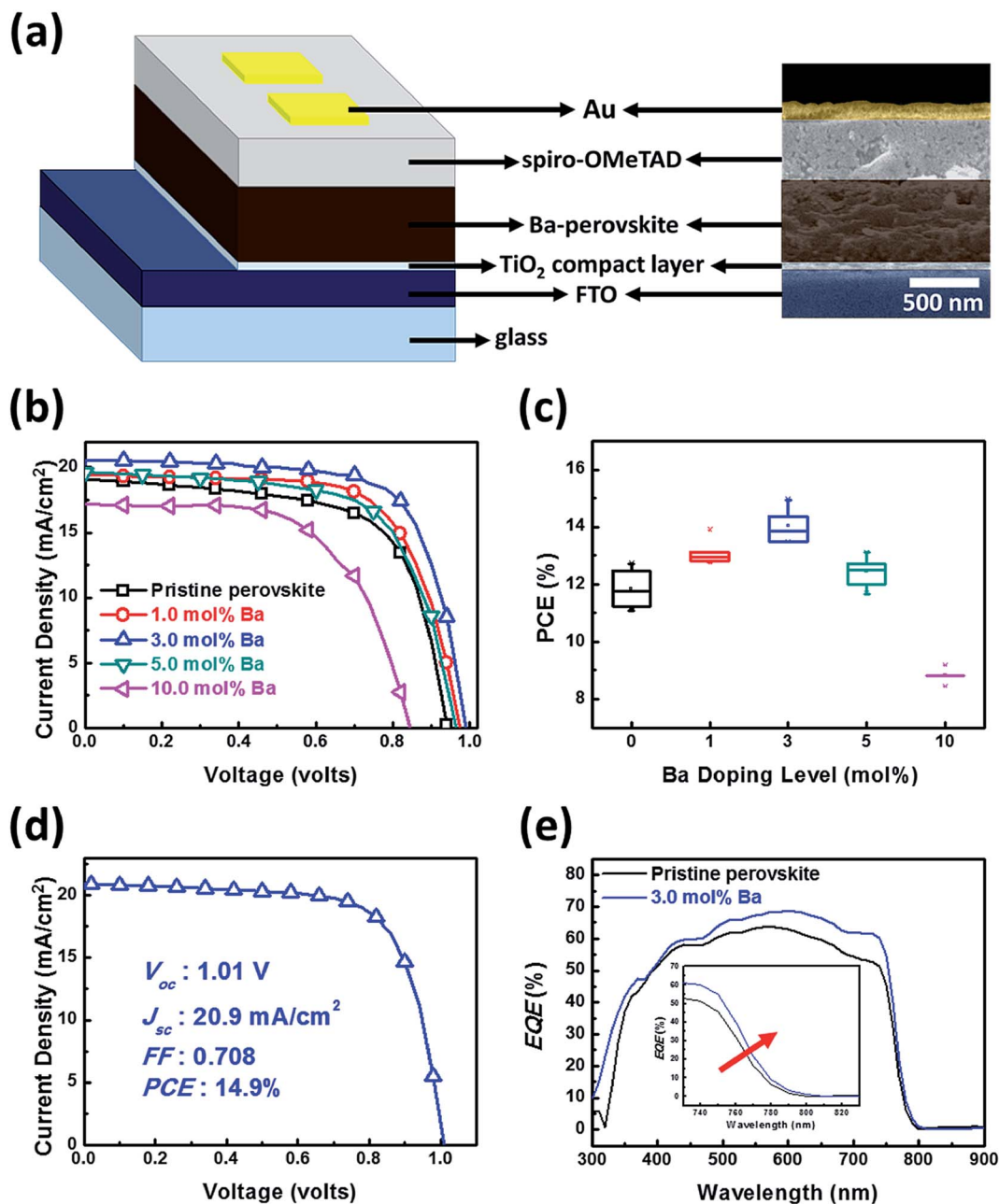
Fig. 7 (a) The schematic diagram and the cross-sectional SEM image of the Ba^{2+}-doped PSC (3.0 mol% sample). (b) The J–V curves and (c) PCE distribution of the PSCs fabricated from the perovskite film without and with various Ba^{2+} doping. (d) The J–V curve of the champion device. (e) EQE spectra of PSCs with either the pristine or 3.0 mol% Ba^{2+}-doped perovskite film.

film annealed at 100 °C shows the highest absorption. However, when the annealing temperature is higher than 120 °C, the absorption is decreased because the perovskite decomposes to PbI$_2$. We further studied the perovskite structure with different annealing temperatures, and the corresponding XRD patterns are shown in Fig. S5(b).† The perovskite film annealed at 100 °C exhibits the highest degree of crystallinity. When the annealing temperature is increased to 160 °C, the perovskite film almost decomposes to PbI$_2$.[41] Fig. 7(b) and (c) show the J–V curves and PCE distribution of solar cells, respectively. The open-circuit voltage (V_{oc}) is slightly increased from 0.95 to 0.99 V with

increasing the Ba^{2+} doping level from 0.0 to 3.0 mol%, because Ba^{2+} doping results in the low electron–hole recombination (Fig. 6(a)). The short-circuit current density (J_{sc}) is increased from 19.2 to 20.4 mA cm^{-2} due to the high absorption behavior (Fig. 3(a)) and improved charge transport (Fig. 6). The solar cells based on the 3.0 mol% Ba^{2+}-doped perovskite film exhibit an average PCE of 14.0% and a champion PCE of 14.9% (Fig. 7(d)). For the solar cells with Ba^{2+} doping larger than 5.0 mol%, they exhibit a low J_{sc} and V_{oc}, because the high Ba^{2+} doping level causes the formation of voids. When the doping level is increased to 10.0 mol%, the PCE is decreased to 8.8%. Hence,

18050 | J. Mater. Chem. A, 2017, 5, 18044–18052

This journal is © The Royal Society of Chemistry 2017

the PCE performance is correlated with the perovskite film morphology and charge transport. From the EQE spectra as shown in Fig. 7(e), the result confirms that the improvement of charge separation efficiency is caused by optimal Ba^{2+} doping concentration. As mentioned, the EQE spectrum of the PSC with 3.0 mol% Ba^{2+} doping exhibits the broad absorption behavior. The chemical compositions of pristine perovskite and 3.0 mol% Ba^{2+}-doped perovskite films were investigated by EDS (Table S1†). The atomic ratios of Ba/Ba + Pb for the 3.0 mol% Ba^{2+}-doped perovskite film is 2.89%.

The instability of the organic–inorganic perovskite structured active layer is a predictable barrier for commercialization.[42,43] In our study, the pristine PSC and 3.0 mol% Ba^{2+}-doped PSC were prepared and stored in the glovebox systems with/without an integrated gas purification system for the stability test. These PSCs were not encapsulated, and they were stored in two kinds of glovebox systems. For the atmosphere of two different glovebox systems, one is N_2 with ~1.0% RH and the other is N_2 with H_2O < 0.1 ppm and O_2 < 0.1 ppm. In the

glovebox systems with the integrated gas purification system (N_2 with H_2O < 0.1 ppm and O_2 < 0.1 ppm), the pristine PSC and 3.0 mol% Ba^{2+}-doped PSC exhibit high stability. After 720 h, these PSCs still possess ~85% of the normalized PCE (Fig. 8(a)). In the glovebox systems without the integrated gas purification system (N_2 with ~1.0% RH), the normalized PCE of the pristine PSC decreases to ~36%, however, the 3.0 mol% Ba^{2+}-doped PSC exhibits ~72% of the normalized PCE (Fig. 8(b)). The result indicates that when the Ba^{2+} doping level is increased to 3.0 mol%, the crystallite size is increased from 75.5 to 91.0 nm. Hence, the larger crystallite size could improve the stability of the PSC.[44]

4. Conclusion

We have investigated the effect of partial replacement of Pb in the perovskite film using alkaline-earth metals ($CH_3NH_3M_{1-x}$-$Pb_xI_{3-y}Cl_y$), where M represents alkaline-earth metals (Mg, Ca, Sr and Ba). The Ba^{2+}-doped perovskite film demonstrates high crystallinity and the highest photovoltaic performance. The optimal doping level of Ba^{2+} was determined by studying the effects of doping levels on the change of the optical absorption behavior, surface morphology, and charge carrier dynamics. When the Ba^{2+} doping level is increased from 0.0 to 3.0 mol%, the crystallinity, absorption behavior, and charge separation efficiency increase with the increased Ba^{2+} doping level. However, a high Ba^{2+} doping level (>3.0 mol%) results in the decay of the properties due to the formation of voids. At the optimal 3.0 mol% Ba^{2+} replacement, the fabricated solar cell shows an average PCE of 14.0% and a champion PCE of 14.9%.

Conflict of interest

There are no conflicts of interest to declare.

Acknowledgements

References

1 M. Saliba, T. Matsui, K. Domanski, J.-Y. Seo, A. Ummadisingu, S. M. Zakeeruddin, J.-P. Correa-Baena, W. R. Tress, A. Abate, A. Hagfeldt and M. Grätzel, *Science*, 2016, **354**, 206–209.

2 M. Saliba, T. Matsui, J.-Y. Seo, K. Domanski, J.-P. Correa-Baena, M. K. Nazeeruddin, S. M. Zakeeruddin, W. Tress, A. Abate, A. Hagfeldt and M. Gratzel, *Energy Environ. Sci.*, 2016, **9**, 1989–1997.
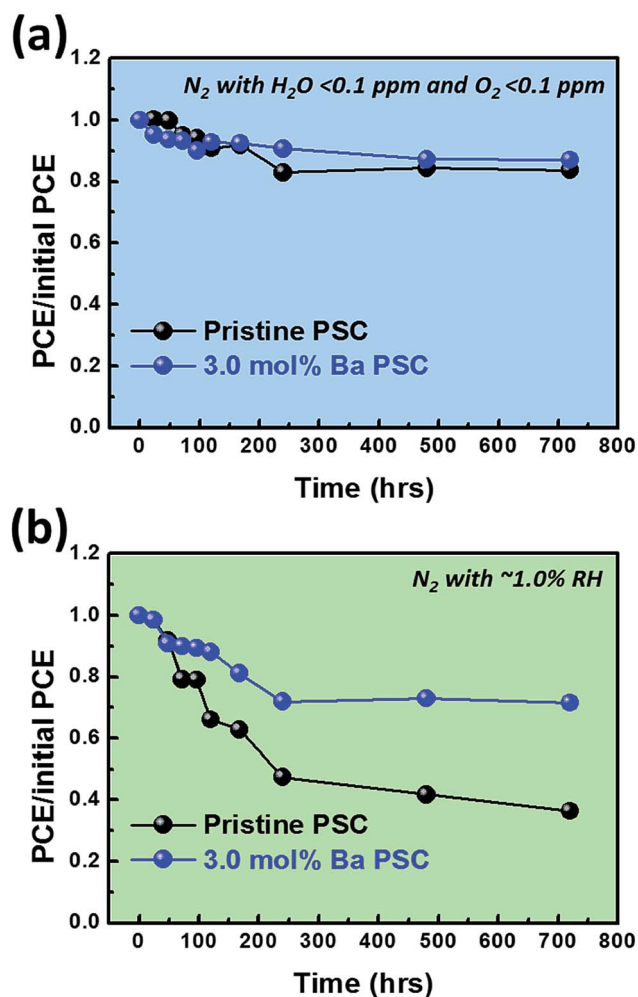

Fig. 8 The stability of PSCs with the pristine and 3.0 mol% Ba^{2+}-doped perovskite films when stored in (a) the glovebox system with the integrated gas purification system and (b) the glovebox system without the integrated gas purification system.

This journal is © The Royal Society of Chemistry 2017

J. Mater. Chem. A, 2017, **5**, 18044–18052 | **18051**

3 N. J. Jeon, J. H. Noh, W. S. Yang, Y. C. Kim, S. Ryu, J. Seo and S. I. Seok, *Nature*, 2015, **517**, 476–480.

4 H.-C. Liao, P. Guo, C.-P. Hsu, M. Lin, B. Wang, L. Zeng, W. Huang, C. M. M. Soe, W.-F. Su, M. J. Bedzyk, M. R. Wasielewski, A. Facchetti, R. P. H. Chang, M. G. Kanatzidis and T. J. Marks, *Adv. Energy Mater.*, 2016, 1601660.

5 A. Kojima, K. Teshima, Y. Shirai and T. Miyasaka, *J. Am. Chem. Soc.*, 2009, **131**, 6050–6051.

6 https://www.nrel.gov/pv/assets/images/efficiency-chart.png.

7 X. Zhang, H. Liu, W. Wang, J. Zhang, B. Xu, K. L. Karen, Y. Zheng, S. Liu, S. Chen, K. Wang and X. W. Sun, *Adv. Mater.*, 2017, 1606405.

8 A. Babayigit, D. Duy Thanh, A. Ethirajan, J. Manca, M. Muller, H.-G. Boyen and B. Conings, *Sci. Rep.*, 2016, **6**, 18721.

9 F. Hao, C. C. Stoumpos, D. H. Cao, R. P. H. Chang and M. G. Kanatzidis, *Nat. Photonics*, 2014, **8**, 489–494.

10 M. H. Kumar, S. Dharani, W. L. Leong, P. P. Boix, R. R. Prabhakar, T. Baikie, C. Shi, H. Ding, R. Ramesh, M. Asta, M. Graetzel, S. G. Mhaisalkar and N. Mathews, *Adv. Mater.*, 2014, **26**, 7122–7127.

11 N. K. Noel, S. D. Stranks, A. Abate, C. Wehrenfennig, S. Guarnera, A.-A. Haghighirad, A. Sadhanala, G. E. Eperon, S. K. Pathak, M. B. Johnston, A. Petrozza, L. M. Herz and H. J. Snaith, *Energy Environ. Sci.*, 2014, **7**, 3061–3068.

12 A. J. Lehner, D. H. Fabini, H. A. Evans, C.-A. Hébert, S. R. Smock, J. Hu, H. Wang, J. W. Zwanziger, M. L. Chabinyc and R. Seshadri, *Chem. Mater.*, 2015, **27**, 7137–7148.

13 F. Giustino and H. J. Snaith, *ACS Energy Lett.*, 2016, **1**, 1233–1240.

14 S. F. Hoefler, G. Trimmel and T. Rath, *Monatsh. Chem.*, 2017, **148**, 795–826.

15 F. Hao, C. C. Stoumpos, P. Guo, N. Zhou, T. J. Marks, R. P. H. Chang and M. G. Kanatzidis, *J. Am. Chem. Soc.*, 2015, **137**, 11445–11452.

16 F. Hao, C. C. Stoumpos, R. P. H. Chang and M. G. Kanatzidis, *J. Am. Chem. Soc.*, 2014, **136**, 8094–8099.

17 J. T.-W. Wang, Z. Wang, S. Pathak, W. Zhang, D. W. deQuilettes, F. Wisnivesky-Rocca-Rivarola, J. Huang, P. K. Nayak, J. B. Patel, H. A. Mohd Yusof, Y. Vaynzof, R. Zhu, I. Ramirez, J. Zhang, C. Ducati, C. Grovenor, M. B. Johnston, D. S. Ginger, R. J. Nicholas and H. J. Snaith, *Energy Environ. Sci.*, 2016, **9**, 2892–2901.

18 J. Navas, A. Sanchez-Coronilla, J. J. Gallardo, N. Cruz Hernandez, J. C. Pinero, R. Alcantara, C. Fernandez-Lorenzo, D. M. De los Santos, T. Aguilar and J. Martin-Calleja, *Nanoscale*, 2015, **7**, 6216–6229.

19 D. Pérez-del-Rey, D. Forgács, E. M. Hutter, T. J. Savenije, D. Nordlund, P. Schulz, J. J. Berry, M. Sessolo and H. J. Bolink, *Adv. Mater.*, 2016, **28**, 9839–9845.

20 M. Pazoki, T. J. Jacobsson, A. Hagfeldt, G. Boschloo and T. Edvinsson, *Phys. Rev. B*, 2016, **93**, 144105.

21 J. Kangsabanik, V. Sharma and A. Alam, *Adv. Mater. Lett.*, 2017, **8**, 342–345.

22 T. J. Jacobsson, M. Pazoki, A. Hagfeldt and T. Edvinsson, *J. Phys. Chem. C*, 2015, **119**, 25673–25683.

23 A. Kumar, K. R. Balasubramaniam, J. Kangsabanik, V. Sharma and A. Alam, *Phys. Rev. B*, 2016, **94**, 180105.

24 M.-C. Wu, S.-H. Chan, M.-H. Jao and W.-F. Su, *Sol. Energy Mater. Sol. Cells*, 2016, **157**, 447–453.

25 D. Liu and T. L. Kelly, *Nat. Photonics*, 2014, **8**, 133–138.

26 J. Cao, F. Wang, H. Yu, Y. Zhou, H. Lu, N. Zhao and C.-P. Wong, *J. Mater. Chem. A*, 2016, **4**, 10223–10230.

27 X. Guo, C. McCleese, C. Kolodziej, A. C. S. Samia, Y. Zhao and C. Burda, *Dalton Trans.*, 2016, **45**, 3806–3813.

28 W. Qiu, T. Merckx, M. Jaysankar, C. Masse de la Huerta, L. Rakocevic, W. Zhang, U. W. Paetzold, R. Gehlhaar, L. Froyen, J. Poortmans, D. Cheyns, H. J. Snaith and P. Heremans, *Energy Environ. Sci.*, 2016, **9**, 484–489.

29 X. Ren, Z. Yang, D. Yang, X. Zhang, D. Cui, Y. Liu, Q. Wei, H. Fan and S. Liu, *Nanoscale*, 2016, **8**, 3816–3822.

30 Q. Chen, N. De Marco, Y. Yang, T.-B. Song, C.-C. Chen, H. Zhao, Z. Hong, H. Zhou and Y. Yang, *Nano Today*, 2015, **10**, 355–396.

31 G. Kieslich, S. Sun and A. K. Cheetham, *Chem. Sci.*, 2015, **6**, 3430–3433.

32 Z. Li, M. Yang, J.-S. Park, S.-H. Wei, J. J. Berry and K. Zhu, *Chem. Mater.*, 2016, **28**, 284–292.

33 M. Yang, T. Zhang, P. Schulz, Z. Li, G. Li, D. H. Kim, N. Guo, J. J. Berry, K. Zhu and Y. Zhao, *Nat. Commun.*, 2016, **7**, 12305.

34 P. Kumar, V. Gulia and A. G. Vedeshwar, *J. Appl. Phys.*, 2013, **114**, 193511.

35 Y. Luo, F. Meng, E. Zhao, Y.-Z. Zheng, Y. Zhou and X. Tao, *J. Power Sources*, 2016, **311**, 130–136.

36 P.-W. Liang, C.-Y. Liao, C.-C. Chueh, F. Zuo, S. T. Williams, X.-K. Xin, J. Lin and A. K. Y. Jen, *Adv. Mater.*, 2014, **26**, 3748–3754.

37 J. You, L. Meng, T.-B. Song, T.-F. Guo, Y. Yang, W.-H. Chang, Z. Hong, H. Chen, H. Zhou, Q. Chen, Y. Liu, N. De Marco and Y. Yang, *Nat. Nanotechnol.*, 2016, **11**, 75–81.

38 R. Ihly, A.-M. Dowgiallo, M. Yang, P. Schulz, N. J. Stanton, O. G. Reid, A. J. Ferguson, K. Zhu, J. J. Berry and J. L. Blackburn, *Energy Environ. Sci.*, 2016, **9**, 1439–1449.

39 N. D. Pham, V. T. Tiong, P. Chen, L. Wang, G. J. Wilson, J. Bell and H. Wang, *J. Mater. Chem. A*, 2017, **5**, 5195–5203.

40 A. Dualeh, N. Tétreault, T. Moehl, P. Gao, M. K. Nazeeruddin and M. Grätzel, *Adv. Funct. Mater.*, 2014, **24**, 3250–3258.

41 S. Luo and W. Daoud, *Materials*, 2016, **9**, 123.

42 J. K. Nam, S. U. Chai, W. Cha, Y. J. Choi, W. Kim, M. S. Jung, J. Kwon, D. Kim and J. H. Park, *Nano Lett.*, 2017, **17**, 2028–2033.

43 J. K. Nam, M. S. Jung, S. U. Chai, Y. J. Choi, D. Kim and J. H. Park, *J. Phys. Chem. Lett.*, 2017, **8**, 2936–2940.

44 C.-H. Chiang and C.-G. Wu, *ChemSusChem*, 2016, **9**, 2666–2672.